

# <sup>1</sup> Differentiable Optics with $\partial$ Lux: I - Deep Calibration of Flat Field and <sup>2</sup> Phase Retrieval with Automatic Differentiation

<sup>3</sup> Louis Desdoigts<sup>a,\*</sup>, Benjamin J. S. Pope<sup>b,c</sup>, Jordan Dennis<sup>b</sup>, Peter G. Tuthill<sup>a</sup>

<sup>4</sup> <sup>a</sup>Sydney Institute for Astronomy, School of Physics, University of Sydney, NSW 2006, Australia

<sup>5</sup> <sup>b</sup>School of Mathematics and Physics, University of Queensland, St Lucia, QLD 4072, Australia

<sup>6</sup> <sup>c</sup>Centre for Astrophysics, University of Southern Queensland, West Street, Toowoomba, QLD 4350, Australia

<sup>7</sup> Send correspondence to L. Desdoigts:

<sup>8</sup> E-mail: [louis.desdoigts@sydney.edu.au](mailto:louis.desdoigts@sydney.edu.au)

<sup>9</sup> Abstract. The sensitivity limits of space telescopes are imposed by uncalibrated errors in the point spread function, photon-  
<sup>10</sup> noise, background light, and detector sensitivity. These are typically calibrated with specialized wavefront sensor hardware and  
<sup>11</sup> with flat fields obtained on the ground or with calibration sources, but these leave vulnerabilities to residual time-varying or  
<sup>12</sup> non-common path aberrations and variations in the detector conditions. It is therefore desirable to infer these from science  
<sup>13</sup> data alone, facing the prohibitively high dimensional problems of phase retrieval and pixel-level calibration. We introduce a  
<sup>14</sup> new Python package for physical optics simulation,  $\partial$ Lux, which uses the machine learning framework Jax to achieve GPU  
<sup>15</sup> acceleration and automatic differentiation ('autodiff'), and apply this to simulating astronomical imaging. In this first of a  
<sup>16</sup> series of papers, we show that gradient descent enabled by autodiff can be used to simultaneously perform phase retrieval  
<sup>17</sup> and calibration of detector sensitivity, scaling efficiently to inferring millions of parameters. This new framework enables high  
<sup>18</sup> dimensional optimization and inference in data analysis and hardware design in astronomy and beyond, which we explore in  
<sup>19</sup> subsequent papers in this series.

## <sup>20</sup> 1 Introduction

<sup>21</sup> At the vanguard of space-based astronomical imaging, photometry, and spectroscopy, imaging precision is  
<sup>22</sup> limited by systematics introduced by aberrations in the optics and noise processes in the detector. While  
<sup>23</sup> problems are ubiquitous in astronomy, we are motivated by several core examples. In exoplanet direct  
<sup>24</sup> imaging, we want to achieve high resolution and high contrast simultaneously with instruments like JWST  
<sup>25</sup> Coronagraphy,<sup>1</sup> Aperture Masking,<sup>2</sup> or Kernel Phase<sup>3,4</sup> modes. The astrometric mission Toliman<sup>5</sup> aims to  
<sup>26</sup> measure precise relative positions of the binary stars  $\alpha$  Centauri AB to reveal the gravitational influence of  
<sup>27</sup> unseen planets; this will require micro-arcsecond, micro-pixel astrometric precision. We may also want to  
<sup>28</sup> perform high precision photometry, whether with dedicated missions like Kepler<sup>6</sup> and TESS,<sup>7</sup> or as ancillary  
<sup>29</sup> science with Toliman.

<sup>30</sup> In each case, we face serious limitations from an imperfect knowledge of the Pixel Response Function  
<sup>31</sup> (PRF) – the map of the intra-pixel and inter-pixel variations in detector sensitivity; and also of the Point  
<sup>32</sup> Spread Function (PSF) – the diffraction-limited pattern by which light from a point source like a star spreads  
<sup>33</sup> across a detector.

<sup>34</sup> In this series of papers, we present a new software package,  $\partial$ Lux, for fitting high-dimensional parametrized  
<sup>35</sup> physical optics models to astronomical data. By using the Python library Jax,<sup>8</sup> we obtain Graphics Processing  
<sup>36</sup> Unit (GPU) hardware acceleration, as well as automatic differentiation or 'autodiff'<sup>9</sup> features that enable  
<sup>37</sup> high-dimensional optimization and inference with gradient descent or Hamiltonian Monte Carlo (HMC<sup>10</sup>). In  
<sup>38</sup> the present paper, we focus on the particular problem of estimating the PRF and PSF simultaneously - i.e.  
<sup>39</sup> joint flat field calibration and phase retrieval. In Paper II, we will show how autodiff enables improvements  
<sup>40</sup> to hardware design, directly calculating and optimizing the Fisher information and therefore fundamental  
<sup>41</sup> figures of merit of an optical system end-to-end. And in subsequent papers, we will use this for end-to-end  
<sup>42</sup> deconvolution of high angular resolution imaging with an unknown PSF. We make  $\partial$ Lux available as open-  
<sup>43</sup> source software on GitHub<sup>1</sup>, and encourage interested readers to use and contribute to this package as a  
<sup>44</sup> community resource. This paper has been compiled using ShowYourWork,<sup>11</sup> so that all figures link to the  
<sup>45</sup> code used to produce them can be found [here](#).

### <sup>46</sup> 1.1 Phase Retrieval

<sup>47</sup> The PSF depends on the successive planes through which light passes from the entrance pupil of the telescope  
<sup>48</sup> through to the detector. This can be calculated from physical optics: for a simple camera bringing light from  
<sup>49</sup> the pupil to focus at a detector plane (the regime of Fraunhofer diffraction), the PSF is the Fourier transform

---

<sup>1</sup>[github.com/LouisDesdoigts/dLux](https://github.com/LouisDesdoigts/dLux)

50 of the input wavefront. In the more general Fresnel regime where the detector is slightly out of focus, there are  
51 additional quadratic phase factors before and after this Fourier transform. In more complicated instruments  
52 like coronagraphs,<sup>12</sup> the light might pass through multiple re-imaged pupil and focal planes, being operated  
53 on in each. In either case, the trouble is that the PSF is distorted by unknown aberrations - distortions in  
54 the wavefront, which can be represented as a spatially-varying phase map across the optical plane.

55 Phase retrieval is the problem of inferring these aberrations from data,<sup>13</sup> which is in general ill-posed:<sup>14</sup>  
56 because of the Hermitian symmetry of the Fourier transform, and because we measure intensity and not  
57 electric field in optical astronomy, there is a large space of aberrations that would generate the same in-  
58 tensity PSF. Fortunately, this space can be restricted to physically-realistic solutions and readily solved by  
59 algorithms such as the Gerchberg-Saxton algorithm,<sup>15</sup> using ideas from compressed sensing,<sup>16</sup> or by ma-  
60 chine learning.<sup>17–19</sup> Phase retrieval was memorably performed to infer and correct the serious aberration  
61 on the Hubble Space Telescope mirror at launch.<sup>20</sup> Earlier work in the vein of this paper has shown that  
62 the phase retrieval problem can be efficiently solved even in the case of detector nonlinearity by taking a  
63 forwards model of physical optics, obtaining partial derivatives with autodiff, and optimizing its parameters  
64 by gradient descent,<sup>21,22</sup> including a conference presentation of an early version of the present work.<sup>23</sup>

## 65 1.2 Detector Calibration

66 High-precision, high-cadence time series of space photometry from Kepler,<sup>6</sup> K2,<sup>24</sup> TESS<sup>25</sup> and CHEOPS<sup>26</sup>  
67 space telescopes have been revolutionary for exoplanetary science<sup>27</sup> and stellar astrophysics.<sup>28,29</sup>

68 In many practical cases, photometric precision is limited by systematic errors due to variations in sensi-  
69 tivity within and between pixels. Changes in telescope pointing or variations in the PSF with focus couple  
70 to these inter- and intra-pixel variations in the flat field to produce changes in overall measured flux. This  
71 was particularly severe for the K2 mission where periodic thruster firings introduced a saw-tooth systematic  
72 on 6 hour timescales, comparable to the durations of exoplanet transits and asteroseismic signals of interest.

73 Much work has been put towards developing data-driven self-calibration of the flat field in K2, which  
74 are of general interest and applicability for other space photometry missions. In Self Flat-Fielding (SFF<sup>30</sup>),  
75 the systematics are modelled with a spline regression of raw flux versus detector position, together with a  
76 linear combination of principal components of all light curves on the detector, and k2sc<sup>31</sup> uses a Gaussian  
77 Process (GP<sup>32,33</sup>) similarly. The Causal Pixel Model (CPM<sup>34</sup>) constrains instrumental effects by measuring  
78 correlations in the light curves of spatially distant, causally-disconnected pixels. In Pixel Level Decorrelation  
79 (PLD<sup>35</sup>) the light curve is detrended by a linear combination of regressors formed by the ensemble of  
80 normalized pixel time series contributing to the light curve, together with their higher-order products.  
81 Halo photometry<sup>36,37</sup> extracts light curves from a weighted sum of pixels where the weights are learned  
82 by minimizing the total variation of the resulting light curve, a convex optimization which is tractable  
83 because of autodiff.

84 Accurate measurement of background noise is also a serious issue for imaging science, where for example  
85 bad pixels, background noise, and uncertainties in the detector systematics limit sensitivity of aperture  
86 masking interferometry and kernel phase,<sup>38</sup> and for low-surface-brightness science such as with Euclid.<sup>39</sup> In  
87 each case it is normal for detectors to be rigorously calibrated on the ground before flight, and with dedicated  
88 observations in space; but at the levels of contrast and resolution required for aperture masking on JWST  
89 (ideally  $10^{-4}$  at a few  $\lambda/D$ ) even small residual miscalibrations can seriously affect performance<sup>2</sup> and we  
90 require some method of self-calibration from science data themselves.

## 91 2 $\partial$ Lux Differentiable Optical Models

92 Rather than working with reduced data products like visibilities and light curves, an alternative is to directly  
93 model the pixel-level images with a parametrized model of the optics and detector. For example, the popular  
94 package poppy<sup>40</sup> can accurately simulate Fresnel and Fraunhofer propagation, with a WebbPSF extension  
95 for preset JWST instrument models.<sup>41</sup> In principle, it is possible to fit such a model to data with Markov  
96 Chain Monte Carlo (MCMC<sup>42</sup>), fitting the positions of stars and a modal basis representation of aberrations;  
97 but common samplers can be very slow, or fail to converge in high dimensions.<sup>43</sup> This restraint is lifted by  
98 using HMC, which requires computation of the gradient of the log-likelihood with respect to parameters.

99 The core technology that enables this for physics also underpins the last decade's revolution in deep  
100 learning:<sup>44</sup> autodiff. By application of the chain rule, it is possible to calculate the partial derivatives of

almost arbitrary numerical functions with respect to their floating-point arguments, so long as they are executed in an appropriate software framework. Considerable private-sector and open-source investment has gone into building autodiff frameworks to enable machine learning, such as Theano,<sup>45</sup> TensorFlow,<sup>46</sup> PyTorch,<sup>47</sup> native support in the Julia language,<sup>48</sup> and the framework we apply in this paper, Jax.<sup>8</sup> Jax has an Application Programming Interface (API) mirroring the common Python array library NumPy,<sup>49</sup> while supporting GPU acceleration, Just-In-Time (jit) compilation, and autodiff.

In this paper we introduce a new optical simulation package,  $\partial$ Lux, available under an open-source BSD license. It significantly extends the capabilities of morphine,<sup>22,50</sup> a previous Jax optics package from our team based on poppy, being rewritten from the ground up taking full advantage of more-recent Jax features and libraries. It is built in an object-oriented Jax framework called zodix which extends equinox<sup>51</sup> for scientific programming. An optical system consisting of an zodix module wrapping a stack of ‘layers’ which are themselves zodix modules applying phase or amplitude screens, or performing Fourier or Fresnel transforms on a wavefront. This allows us to re-frame the idea of a computational optical model by analogy to a ‘parametrized neural network’, with each operation performed on the wavefront analogous to a neural network layer encoding the physics of the transformation. The object-oriented nature of zodix allows for larger and more complex models to be built and seamlessly integrated than would be possible within the purely functional framework default to Jax. zodix is also built to be directly integrated into the Jax framework, allowing for all Jax functions to seamlessly interface with any zodix models and vice-versa. Talk about zodix too? We use the optimization library optax<sup>52</sup> for gradient-descent optimization, and the probabilistic programming library numpyro<sup>53</sup> for HMC.

There are several other frameworks for automatically-differentiable optics simulation: the most similar is WaveBlocks,<sup>54</sup> a PyTorch package for object-oriented modelling of fluorescence microscopy. The DeepOptics package<sup>55</sup> has been developed in TensorFlow for camera design and computational imaging, and WaveDiff in TensorFlow has been used for detector calibration<sup>56</sup> and PSF modelling.<sup>57</sup> We believe that  $\partial$ Lux fills a unique niche in this ecosystem as the most general modelling framework for physical optics. This has driven a design focus on flexibility and ease of open-source contribution and development. The goal is to provide a general object-oriented framework that enables a new user to harness the advantages of autodiff and hardware acceleration provided by Jax with its user-friendly NumPy-like API.

### 129 3 Optical and Instrumental Modelling

Within the  $\partial$ Lux framework we explicitly define each operation applied to the wavefront as a unique layer. Here we employ a simple optical model with only a pupil and focal plane, defined by 6 sequential layers. Here we show how to create this optical system within the  $\partial$ Lux framework:

```

133
134 import jax.numpy as np
135 import jax.random as jr
136 import dLux as dl
137
138 # Define wavelengths
139 wavels = 1e-9 * np.linspace(545, 645, 3)
140
141 # Basic Optical Parameters
142 aperture = 0.5
143 wf_npix = 512
144
145 # Detector Parameters
146 det_npix = 1024
147 sampling_rate = 20
148 det_pixsize = dl.utils.get_pixel_scale(sampling_rate, wavels.mean(), aperture)
149
150 # Zernike Basis (ignore piston, tip, tilt)
151 noll_inds = np.arange(4, 11)
152 coeffs = 2e-8 * jr.normal(jr.PRNGKey(1), (len(noll_inds),))
153
  
```

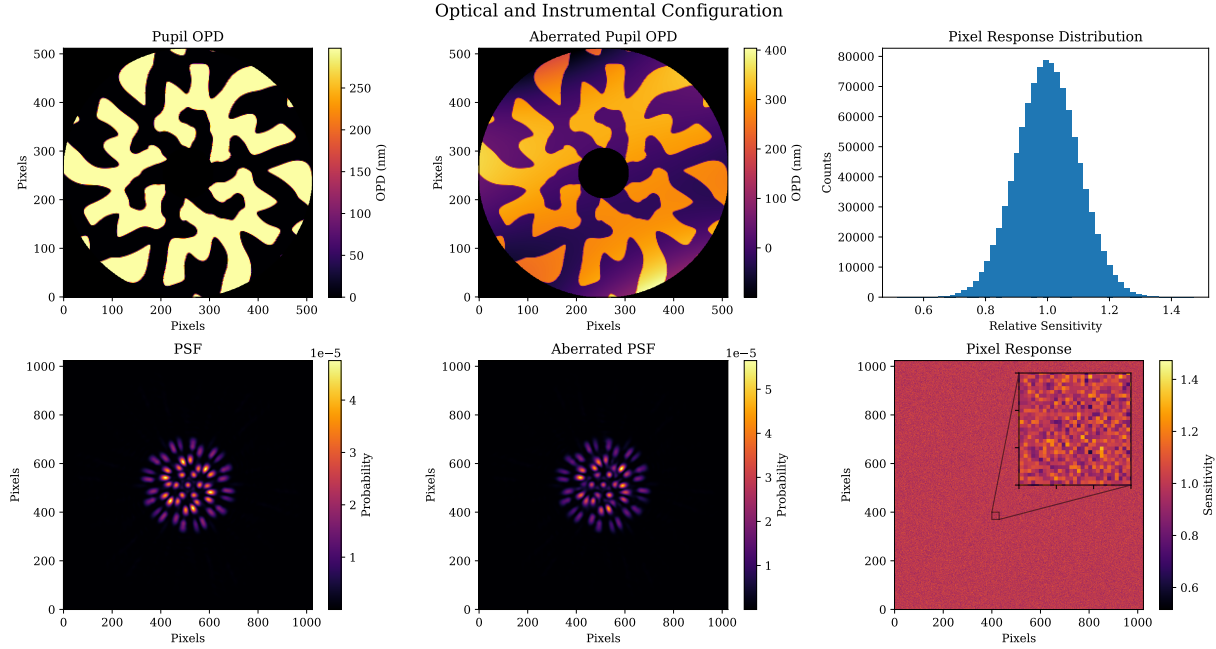


Fig 1 Summary of the optical configuration. Left panel: The top plot show the Optical Path Difference (OPD) of the pupil at the aperture of the telescope. The binary values create a half-wave step at the mean observation wavelength. The bottom plot shows the resulting large single-star PSF without aberrations applied. Middle panel: The top plot shows the total Optical Path Difference (OPD) of the pupil with the optical aberrations applied using low-order Zernike polynomials that is used to generate the data. The bottom plot shows the resulting single-star PSF with the aberrations applied. Clearly these aberrations have a large effect on the PSF and would make recovering information very difficult without appropriate calibration. Right panel: The top plot shows the histogram of the PRF that is applied in the focal plane. These values have a large spread and would greatly affect any results without calibration. The bottom plot shows the full PRF across the whole detector, with a small zoomed region used to show the fine detail that can not be seen when examining the full detector.

```

154 # Define Optical Configuration
155 layers = [
156     d1.CreateWavefront    (wf_npix , aperture) ,
157     d1.ApertureFactory    (wf_npix , secondary_ratio=0.2) ,
158     d1.AberrationFactory  (wf_npix , zernikes=noll_inds , coefficients=coeffs) ,
159     d1.AddOPD              (np.load("mask.npy")) ,
160     d1.NormaliseWavefront () ,
161     d1.AngularMFT         (det_npix , det_pixsize) ]
162
163 # Create Optics object
164 optics = d1.Optics(layers)

```

The first layer creates our wavefront and the second modifies the amplitude to model its response to the transmission of the aperture.

The wavefront then encounters low-order phase errors parameterised by coefficients on Zernike polynomials. We include the first 4 radial terms, ignoring global piston, tip and tilt for a total of 7 terms. Coefficients were randomly drawn from a normal distribution of mean 0 and standard deviation 20 nm. These aberrations applied to the pupil mask and resulting PSF are shown in the middle panel of Figure 1, where we see this induces a large amount of distortion in the PSF.

Next the wavefront encounters the binary phase plate diffractive pupil from Toliman,<sup>5</sup> with a half-wave total Optical Path Difference (OPD) between the binary regions. We use this as an information-preserving way to spread the PSF across a large number of pixels which encodes the PRF information for a large number of pixels simultaneously. Alternative methods such as defocusing or using a diffuser<sup>58</sup> come at the cost of

177 eliminating Fourier information which constrain the wavefront and positions. An important consideration  
178 which is alleviated by the Tolimán pupil is that focal-plane wavefront sensing suffers a sign ambiguity for  
179 all phase modes that are inversion-symmetric about the origin, and for unambiguous phase retrieval we  
180 therefore need an asymmetric or odd-mode symmetric pupil.<sup>59</sup> This pupil and corresponding aberrated PSF  
181 are shown in the left panel of Figure 1.

182 This is then propagated to the  $1024 \times 1024$  pixel focal plane by a two-sided matrix Fourier transform.<sup>60,61</sup>  
 183 The detector PRF is modelled by multiplying the resulting PSF by a pixel sensitivity map which is drawn  
 184 from a normal distribution with mean 0 and standard deviation 0.1. The histogram of pixel sensitivities and  
 185 total pixel sensitivity map is shown in the right panel of Figure 1. Here we show how to create this within  
 186 the  $\partial$ Lux framework and create an instrument object to model this:  
 187

```

188 # Pixel response
189 pix_response = 1 + 0.1* jr .normal( jr .PRNGKey(2) , [det_npix , det_npix])
190
191 # Create Detector object
192 detector = dl.Detector([dl.ApplyPixelResponse(pix_response)])
193
194 # Combine into instrument
195 tel = dl.Instrument(optics , detector=detector)
  
```

197 This operation is then performed over 20 stars with uniform 100 nm bandpass spectra sampled at three  
 198 wavelengths 545 nm, 595 nm and 645 nm. This total model requires the calculation of 60 individual PSFs  
 199 over a  $1024 \times 1024$  detector from a  $512 \times 512$  pixel wavefront. This calculation is vastly dominated by  
 200 the propagation of the wavefront using a 2-sided MFT, which requires two matrix multiplications for each  
 201 individual PSF of sizes  $[N_o \times N_i] \cdot [N_i \times N_i]$  and  $[N_o \times N_i] \cdot [N_i \times N_o]$  where  $N_i = 512$  is the input size of the  
 202 wavefront and  $N_o = 1024$  is the output size of the wavefront. This takes a total of  $\sim 1.25$  seconds to evaluate  
 203 on an Apple M1 CPU, with all operations performed using FP32 precision default to Jax. FP32 was chosen  
 204 as this problem does not require precision over a large dynamic range, however FP64 calculations can be  
 205 performed as required. We also apply 4 integer-pixel dithers of  $\pm 20$  pixels in the (x,y) directions, equivalent  
 206 to a  $1 \lambda/D$  dither for a total of 5 images with the total flux spread evenly across each image. This helps the  
 207 over-parameterisation consequential from having a free parameter for each pixel. Using pixel-integer dithers  
 208 similarly allows for a single PSF calculation on a slightly larger detector plane (1064x1064 in this case) and  
 209 then sampling the smaller 1024x1024 regions to produce the full set of 5 images.

210 The data set is generated by taking this set of images and applying Poisson photon noise to the PSFs. Using  
 211 this image we recover stellar positions and fluxes, optical aberrations, and individual pixel sensitivities. This  
 212 gives us 40 stellar positional parameters (20 RA and DEC each), 20 stellar flux parameters, 7 optical  
 213 aberration parameters, and 1,048,576 detector parameters: the dimensionality of the problem is vastly  
 214 dominated by the PRF parameters, which is why this problem is made tractable only by using autodiff.

#### 215 4 Optimisation and Results: Phase Retrieval and Flat Field Estimation

216 To recover these parameters we initialise a naive unaberrated optical model with a uniform PRF. Stellar  
 217 positions were perturbed by adding a random value drawn from a normal distribution mean 0 deviation  
 218 1 pixel and fluxes were perturbed by multiplying their value by a random value drawn from a normal  
 219 distribution mean 1 deviation 0.1. We will use this model to recover the true values. Figure 2 shows the  
 220 data and the initial and final residuals.

221 In order to recover these input aberrations, we perform gradient descent using Adam<sup>62</sup> as implemented  
 222 in optax,<sup>52</sup> minimizing the posterior of a per-pixel Poisson log-likelihood with a  $\chi^2$  log prior on the PRF  
 223 values, matching the true distribution of mean 1 deviation 0.1. We take the gradient of this loss function  
 224 with respect to the position and flux of all stars, the response in all pixels, and the Zernike coefficients.  
 225 We also use a staged optimisation strategy, initially optimising the positions, fluxes and optical aberrations  
 226 in order to recover a good PSF model before learning the PRF. This is necessary to circumvent the high  
 227 degree of covariance that each individual pixel experiences with the parameters of the PSF. To achieve this  
 228 the learning rate of the PRF is set to zero for the first 100 epochs of optimisation, after which the PRF  
 229 learning rate is initialised while the position, flux and aberrations parameters are frozen for the remaining  
 230 50 epochs. This helps to circumvent the global covariance between the mean PRF and flux which can result  
 231 in an overestimation of the flux parameters as the model tries to fit to the noise.

232 The optimisation is performed for a total of 150 epochs, with each value-and-gradient calculation taking  
 233  $\sim 2.75$  seconds to evaluate on an Apple M1 Max CPU, for a total optimisation time of  $\sim 6.5$  minutes. Faster  
 234 convergence can be achieved by careful tuning of the optimisation hyper-parameters such as learning rate

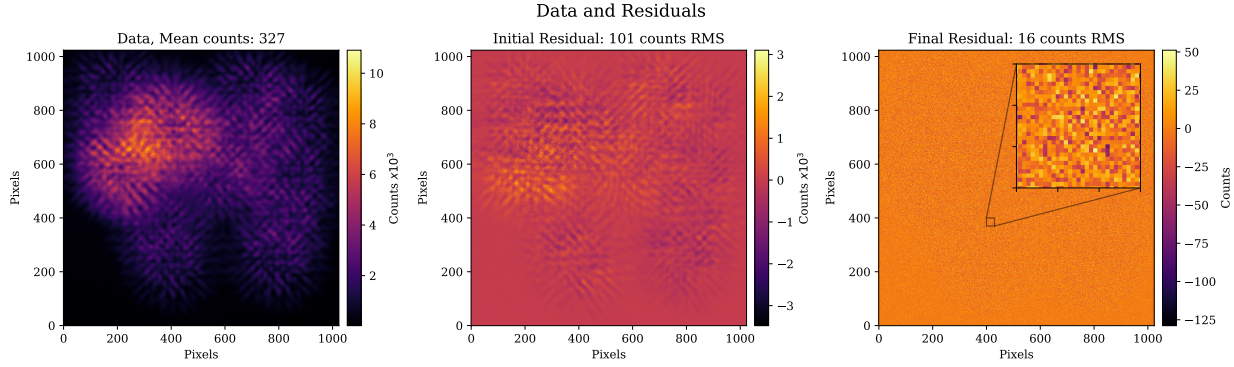


Fig 2 Left: The sum of the images from which the PRF is recovered. By eye it is clearly difficult to disentangle the astrophysical information. The large number of overlapping PSFs is chosen in order to spread light across the majority of the detector so that we encode the PRF information for as much of the detector as possible. Middle: The sum of the residual of the data and the initial uncalibrated model. Clearly these residuals are large, showing that there is a large amount of calibration required. Right: This same residual after the model has been optimised. The residual values are much smaller with no discernable structure remaining. A small zoomed region is shown so that the individual pixel-level residuals can be seen.



### Astrophysical Parameters

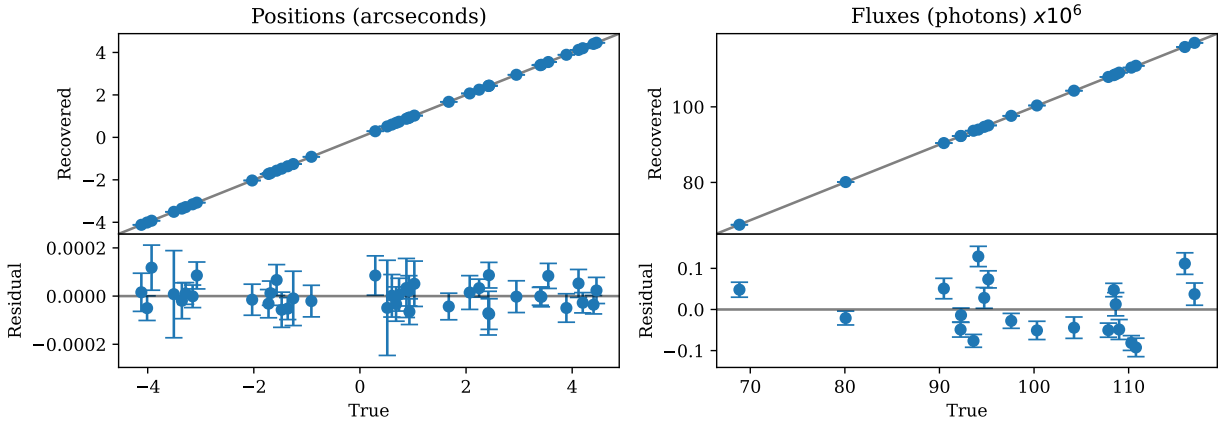


Fig 3 Left: recovery of the individual RA-Dec positions of each star, with the top section showing the correlation between the true and recovered values in units of arcseconds. The bottom section shows the individual residuals for each. Clearly these parameters have been well recovered through the optimisation. Right: the recovery of the flux parameters in units of photons. The top section shows the correlation between the true and recovered values, and the bottom showing the resulting residuals. The error bars are the  $1-\sigma$  deviations calculated from the covariance Hessian matrix marginalised over positions, fluxes and aberrations.



and momentum, however we take a slower approach in this work in order to get good performance across a range of fluxes and PRFs which is analysed in Section 5.

This optimisation strategy performs well, with Figure 2 showing the final residual image with no visually discernable structure. A further analysis of parameter recovery over a range of fluxes and PRFs is shown in Section 5. Correlations and residual plots of the positions, fluxes and aberrations after the optimisation are shown in Figure 3 and Figure 4. Figure 4 shows the recovery of the optical aberrations, with a final residual aberration of 0.0282 nm RMS.

Finally, Figure 5 shows a correlation plot of the true and recovered sensitivity values and the corresponding residual histogram. The points of the correlation plot are colour-coded with the total counts for each pixel, showing as expected that pixels with higher photon counts having a better recovery of the PRF since these pixels have a greater signal-to-noise ratio (SNR). Overall the parameters are very well recovered down to the noise level.

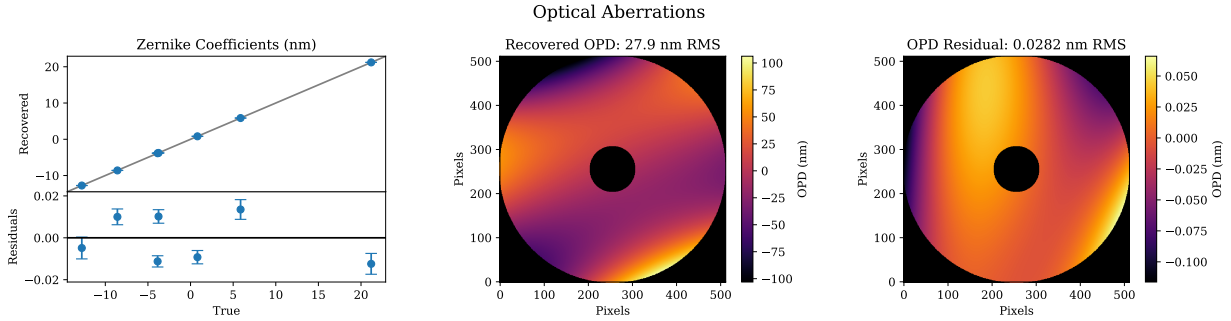


Fig 4 Recovery of the optical aberrations after optimisation. Left: the amplitudes of the Zernike polynomial coefficients, with the top section showing the correlation plot of the true and recovered values, and the bottom showing the individual residuals. Middle and right: the true total OPD and the residuals generated by these values respectively. The error bars are the  $1-\sigma$  deviations calculated from the covariance Hessian matrix marginalised over positions, fluxes and aberrations.

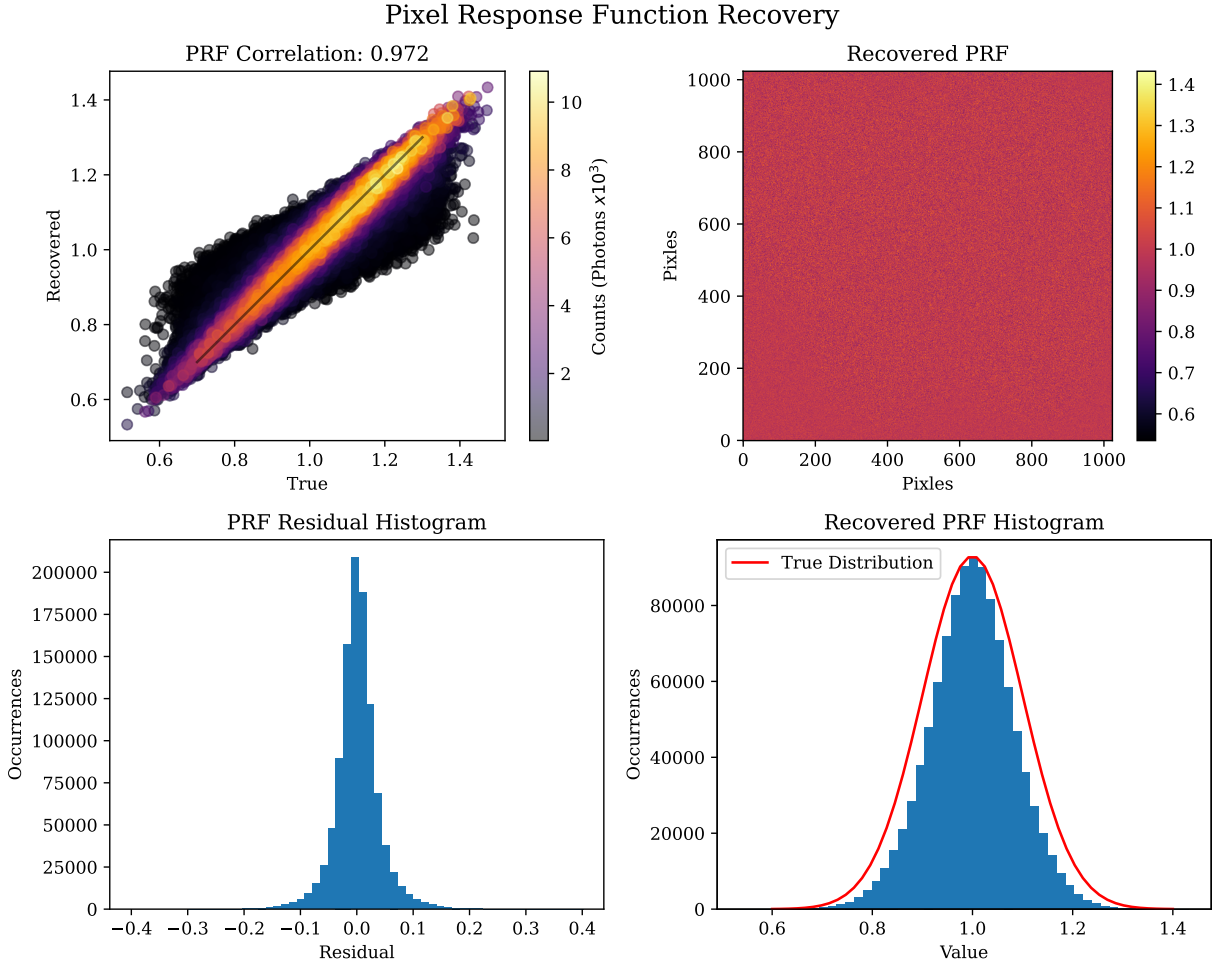


Fig 5 PRF values after optimisation. Left: Correlation between the pixel-level true and recovered values. Each point is color-coded with the total flux incident to each pixel, ie its SNR. The pixels with a greater signal are recovered better as expected. Right: Histogram of these residuals, with the majority of values being very well recovered and small symmetric about a residual of zero.

247 We can also leverage the differentiability of these models in order to estimate the errors in these parameters  
 248 under the Laplace approximation,<sup>63</sup> by taking the inverse Hessian of the Poisson likelihood. Using this  
 249 method marginalised errors can be calculated incorporating parameter covariance. There are some limitations  
 250 using this method as it requires the calculation of the covariance matrix over all parameters - which in this  
 251 model is over a million, giving a covariance matrix of over a computationally-intractable trillion values.  
 252 Instead we calculate the errors marginalising only over stellar positions, fluxes and optical aberrations, with  
 253 pixel sensitivities held constant. This provides us with an accurate calculation of the true errors when photon  
 254 noise is dominant, but it will remain an underestimate when the PRF is the dominant noise source. We  
 255 chose to estimate our errors in this manner as opposed to the conventional photon-noise scaling relations in  
 256 order to better capture covariance between parameters. In Section 5 we provide a comprehensive analysis of  
 257 our results with respect to these photon-noise scaling relations.

258 The use of a forwards model clearly requires a good match between the true and model PSF. The benefit  
 259 of using differentiable optical models however is that it provides the perfect platform upon which to directly  
 260 learn this model from the data, with the ability to scale the complexity as required for each problem. Similarly  
 261 since we are working with direct image data as opposed to reduced data-products, miss-calibrations of the  
 262 system are simple to diagnose through direct examination of the residuals of the data and model. Figure 2  
 263 demonstrates that in this example we can be sure of a good fit because the final residual contains no visually  
 264 identifiable structure.

## 265 5 Noise & Performance Analysis

266 This section examines how well this method performs across a range of both PRF and flux values, which  
 267 are our two dominant noise sources. Recovering parameters in a Poisson-noise-dominated regime for simple  
 268 optical systems should have the following relationships:

$$\sigma_{\text{flux}} = 1/\sqrt{N_{\text{phot}}} \text{ (photons)}$$

$$\sigma_{\text{position}} = \frac{1}{\pi} \sqrt{2/N_{\text{phot}}} \frac{\lambda}{D} \text{ (radians)}$$

$$\sigma_{\text{zernike}} = 1/\sqrt{N_{\text{phot}}} \text{ (RMS radians)}$$

269 Comparing the errors in the recovered parameters across a range of fluxes provides a good way to examine  
 270 when we are in the photon noise dominated regime. After optimisation the errors are calculated for each  
 271 parameter and compared to these expected values. ie:

$$\sigma_{\text{relative}} = \sum_{i=1}^N \frac{1}{N} \frac{\sigma_i \text{ recovered}}{\sigma_i \text{ expected}}$$

272 The top-left panel of Figure 6 shows the weighted Pearson correlation coefficient<sup>64</sup> as a function of both  
 273 flux and PRF. The transition where the PRF is recoverable denotes two regimes: one where photon noise  
 274 dominates and another where PRF noise dominates. We have distinct results in these different regimes.  
 275 Astrophysical and optical parameters are recovered to the photon noise expectation, while there is poor  
 276 recovery of the PRF when photon noise is the dominant source and vice versa when the PRF is the dominant  
 277 noise source. The top-right and bottom panels of Figure 6 show how  $\sigma_{\text{relative}}$  changes as a function of both  
 278 flux and PRF. These  $\sigma_{\text{expected}}$  values are expected to be underestimates of the true values because they are  
 279 not marginalised over all of the fitted parameters in the forwards model. By examining Figure 6, we can see  
 280 that there is a transition between two regimes: photon noise dominated and PRF noise dominated. In the  
 281 photon noise dominated regime, we can see that the parameters are recovered to the level expected by these  
 282 relationships and diverge from these once the PRF becomes the primary noise source.

283 It is important to note in this section that there is a degree of scatter in the recovered results. Due to the  
 284 gradient descent optimisation strategy there is a degree of sensitivity to the optimisation hyper-parameters,  
 285 such as learning rates which must be tuned based on the flux, momentum, and distance to the noise floor.  
 286 These parameters are simple enough to tune for individual data sets with similar scales, but it is non-trivial

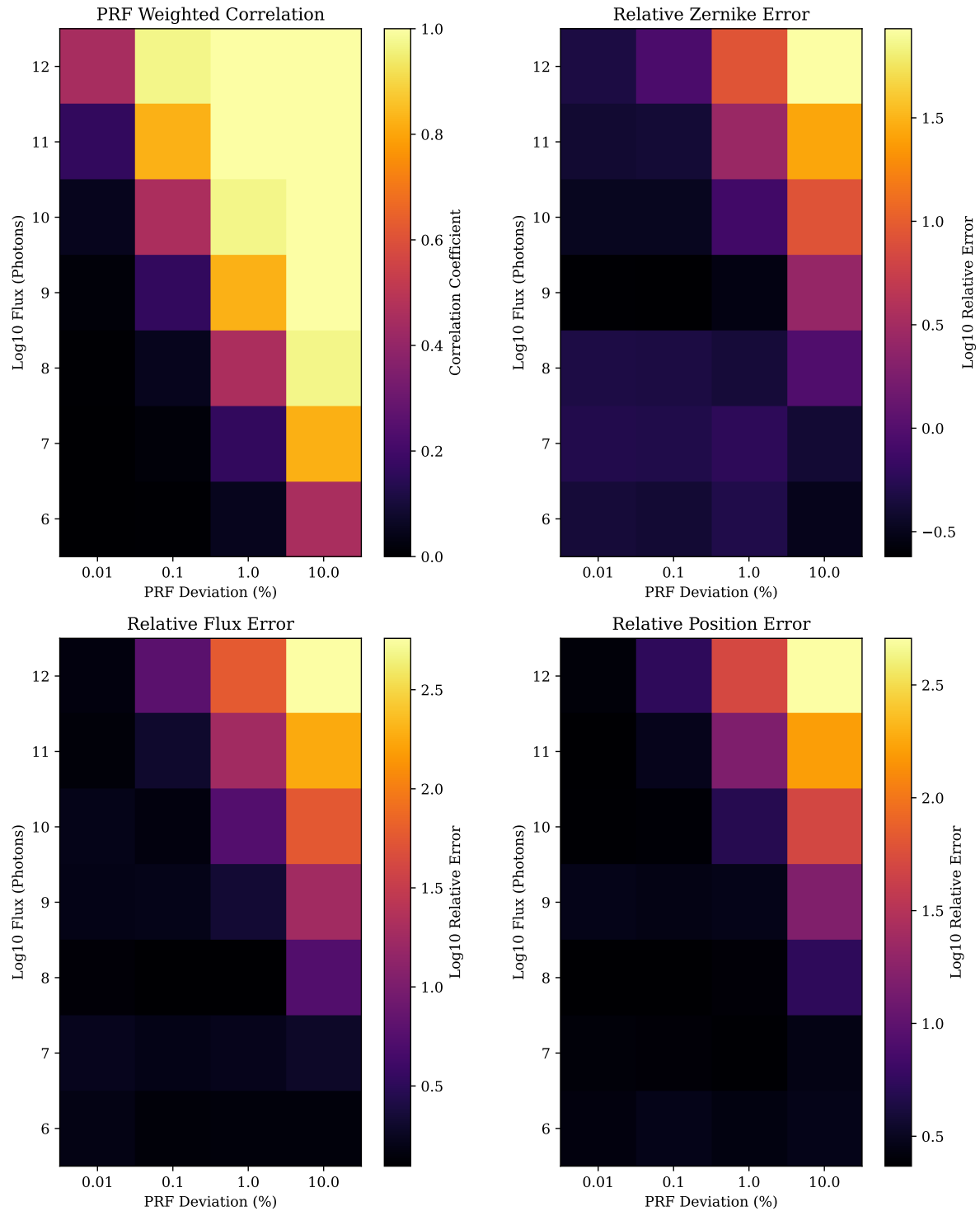


Fig 6 Recovered parameter error relative to photon noise expectation. Left: Mean relative per-mode Zernike error. Middle: Mean relative flux error. Right: Mean relative positional error.

287 to automate this process for data with a vast range of scales like those being analysed here. The hyper-  
288 parameters chosen were tuned on the 1e8 flux data set and roughly scaled to work with the other data  
289 sets, which is why we observe the best recovery for that set of parameters. These figures are designed to  
290 demonstrate the overall trends in the different noise regimes, rather than to be a precise analysis of the  
291 fundamental limits.

## 292 6 Conclusions & Future Work

293 In this first paper of a planned series, we have demonstrated photometry, phase retrieval, and detector  
294 calibration using autodiff to make tractable gradient descent in very high dimensions. Our software  $\partial$ Lux  
295 integrates with a rich and user-friendly ecosystem of Jax packages for optimization and sampling, which  
296 point to a number of natural extensions.

297 The most obvious is to produce calibrated photometric time series, making use of correlations in time  
298 rather than the ‘bag of images’ approach taken in this work. Instead of independently optimizing each frame,  
299 they could be treated hierarchically, with regularization imposed on each star’s light curve. GP models are  
300 widely used in astronomy, and Jax packages such as tinygp<sup>33</sup> and GPJax<sup>65</sup> permit differentiable optimization  
301 and sampling that integrate efficiently with  $\partial$ Lux.

302 Photometry of crowded fields is often of poor quality even from space telescopes, and there has been  
303 considerable investment in algorithms for deblending light curves in the K2 galactic plane campaigns<sup>66</sup>  
304 and in TESS with its large pixels.<sup>67–69</sup> High dimensional optimization with autodiff in principle renders  
305 deblending tractable even close to the diffraction limit with unknown PSFs. Prior knowledge of a structured  
306 PSF, such as with the diffractive pupil architecture of Toliman,<sup>70,71</sup> may further improve this deblending  
307 and retrieval.

308 High-precision photometric measurements often need to also consider variations in the intra-pixel sensitivity.  
309 This work only examined the inter-pixel sensitivity for simplicity, however the PSFs examined here  
310 were sampled at 10x the Nyquist limit, well beyond the typical 1-1.5x Nyquist used in practice. The ability  
311 to recover sensitivity variations over these sub-fringe scales show that this method can be directly applied  
312 to recovery of both inter and intra-pixel sensitivity fluctuations.

313 High contrast imaging with the recently-launched JWST<sup>72</sup> and the upcoming Roman Space Telescope  
314 coronagraph<sup>73</sup> will in each case demand a new generation of data-driven PSF and detector calibrations  
315 beyond those used fruitfully on ground-based data.<sup>74</sup> While we have not attempted this in the present work,  
316  $\partial$ Lux can flexibly model aberrations in the multiple intermediate planes of these coronagraphs, and in future  
317 work we intend to assess the practical and fundamental limits of multiplane phase retrieval and calibration  
318 to improve coronagraphic modelling. Uncertainties in the flat field are also the leading contributor to noise  
319 in the exoplanet transmission spectroscopy with JWST,<sup>75</sup> and a promising future direction with  $\partial$ Lux will  
320 be to build models not just of imaging data, but of spectrophotometry.

321 In Paper II in this series, we will tackle the isomorphic problem of hardware design. While we have  
322 tackled phase design in previous work,<sup>22</sup> autodiff permits calculation and optimization of the Fisher information  
323 directly,<sup>76</sup> which means we can optimize towards the fundamental limits of parameter sensitivity.  
324 In subsequent papers, we intend to explore parametric and nonparametric deconvolution of images at high  
325 angular resolution and contrast.

## 326 7 Acknowledgements

327 We thank Laurent Pueyo and Tim White for their helpful discussions.

328 We acknowledge and pay respect to the Gadigal people of the Eora Nation, upon whose unceded,  
329 sovereign, ancestral lands the University of Sydney is built; and the traditional owners of the land on  
330 which the University of Queensland is situated, the Turrbal and Jagera people. We pay respects to their  
331 Ancestors and descendants, who continue cultural and spiritual connections to Country.

332 This research made use of NumPy,<sup>49</sup> Matplotlib;<sup>77</sup> Jax;<sup>8</sup> equinox;<sup>51</sup> and optax.<sup>52</sup>

## 333    References

- 334    1 J. H. Girard, J. Leisenring, J. Kammerer, M. Gennaro, M. Rieke, J. Stansberry, A. Rest, E. Egami,  
 335    B. Sunnquist, M. Boyer, A. Canipe, M. Correnti, B. Hilbert, M. D. Perrin, L. Pueyo, R. Soummer,  
 336    M. Allen, H. Bushouse, J. Aguilar, B. Brooks, D. Coe, A. DiFelice, D. Golimowski, G. Hartig, D. C.  
 337    Hines, A. Koekemoer, B. Nickson, N. Nikolov, V. Kozhurina-Platais, N. Pirzkal, M. Robberto, A. Sivar-  
 338    amakrishnan, S. T. Sohn, R. Telfer, C. R. Wu, T. Beatty, M. Florian, K. Hainline, D. Kelly, K. Misselt,  
 339    E. Schlawin, F. Sun, C. Williams, C. Willmer, C. Stark, M. Ygouf, A. Carter, C. Beichman, T. P. Greene,  
 340    T. Roellig, J. Krist, J. Adams Redai, J. Wang, C. R. Clark, D. Lewis, and M. Ferry, "JWST/NIRCam  
 341    coronagraphy: commissioning and first on-sky results," in Space Telescopes and Instrumentation 2022:  
 342    Optical, Infrared, and Millimeter Wave, L. E. Coyle, S. Matsuura, and M. D. Perrin, eds., Society of  
 343    Photo-Optical Instrumentation Engineers (SPIE) Conference Series 12180, p. 121803Q, Aug. 2022.
- 344    2 A. Sivararamakrishnan, P. Tuthill, J. P. Lloyd, A. Z. Greenbaum, D. Thatte, R. A. Cooper, T. Van-  
 345    dandal, J. Kammerer, J. Sanchez-Bermudez, B. J. S. Pope, D. Blakely, L. Albert, N. J. Cook, D. John-  
 346    stone, A. R. Martel, K. Volk, A. Soulain, É. Artigau, D. Lafrenière, C. J. Willott, S. Parmentier,  
 347    K. E. S. Ford, B. McKernan, M. Begoña Vila, N. Rowlands, R. Doyon, L. Desdoigts, A. W. Fullerton,  
 348    M. De Furio, P. Goudfrooij, S. T. Holfeltz, S. LaMassa, M. Maszkiewicz, M. R. Meyer, M. D. Perrin,  
 349    L. Pueyo, J. Sahlmann, S. T. Sohn, and P. S. Teixeira, "The Near Infrared Imager and Slitless Spec-  
 350    trograph for the James Webb Space Telescope – IV. Aperture Masking Interferometry," arXiv e-prints  
 351    , p. arXiv:2210.17434, Oct. 2022.
- 352    3 F. Martinache, "Kernel Phase in Fizeau Interferometry," ApJ 724, pp. 464–469, Nov. 2010.
- 353    4 J. Kammerer, R. A. Cooper, T. Vandal, D. Thatte, F. Martinache, A. Sivararamakrishnan, A. Chaushev,  
 354    T. Stolker, J. P. Lloyd, L. Albert, R. Doyon, S. Sallum, M. D. Perrin, L. Pueyo, A. Mérand, A. Gallenne,  
 355    A. Greenbaum, J. Sanchez-Bermudez, D. Blakely, D. Johnstone, K. Volk, A. Martel, P. Goudfrooij, M. R.  
 356    Meyer, C. J. Willott, M. De Furio, L. Dang, M. Radica, and G. Noiro, "The Near Infrared Imager  
 357    and Slitless Spectrograph for JWST – V. Kernel Phase Imaging and Data Analysis," arXiv e-prints ,  
 358    p. arXiv:2210.17528, Oct. 2022.
- 359    5 P. Tuthill, E. Bendek, O. Guyon, A. Horton, B. Jeffries, N. Jovanovic, P. Klupar, K. Larkin, B. Nor-  
 360    rris, B. Pope, and M. Shao, "The TOLIMAN space telescope," in Optical and Infrared Interferometry  
 361    and Imaging VI, M. J. Creech-Eakman, P. G. Tuthill, and A. Mérand, eds., 10701, pp. 432 – 441,  
 362    International Society for Optics and Photonics, SPIE, 2018.
- 363    6 W. J. Borucki, D. Koch, G. Basri, N. Batalha, T. Brown, D. Caldwell, J. Caldwell, J. Christensen-  
 364    Dalsgaard, W. D. Cochran, E. DeVore, E. W. Dunham, A. K. Dupree, T. N. Gautier, J. C. Geary,  
 365    R. Gilliland, A. Gould, S. B. Howell, J. M. Jenkins, Y. Kondo, D. W. Latham, G. W. Marcy, S. Meibom,  
 366    H. Kjeldsen, J. J. Lissauer, D. G. Monet, D. Morrison, D. Sasselov, J. Tarter, A. Boss, D. Brownlee,  
 367    T. Owen, D. Buzasi, D. Charbonneau, L. Doyle, J. Fortney, E. B. Ford, M. J. Holman, S. Seager,  
 368    J. H. Steffen, W. F. Welsh, J. Rowe, H. Anderson, L. Buchhave, D. Ciardi, L. Walkowicz, W. Sherry,  
 369    E. Horch, H. Isaacson, M. E. Everett, D. Fischer, G. Torres, J. A. Johnson, M. Endl, P. MacQueen, S. T.  
 370    Bryson, J. Dotson, M. Haas, J. Kolodziejczak, J. Van Cleve, H. Chandrasekaran, J. D. Twicken, E. V.  
 371    Quintana, B. D. Clarke, C. Allen, J. Li, H. Wu, P. Tenenbaum, E. Verner, F. Bruhweiler, J. Barnes,  
 372    and A. Prsa, "Kepler Planet-Detection Mission: Introduction and First Results," Science 327, p. 977,  
 373    Feb. 2010.
- 374    7 G. R. Ricker, J. N. Winn, R. Vanderspek, D. W. Latham, G. Á. Bakos, J. L. Bean, Z. K. Berta-  
 375    Thompson, T. M. Brown, L. Buchhave, N. R. Butler, R. P. Butler, W. J. Chaplin, D. Charbonneau,  
 376    J. Christensen-Dalsgaard, M. Clampin, D. Deming, J. Doty, N. De Lee, C. Dressing, E. W. Dunham,  
 377    M. Endl, F. Fressin, J. Ge, T. Henning, M. J. Holman, A. W. Howard, S. Ida, J. M. Jenkins, G. Jernigan,  
 378    J. A. Johnson, L. Kaltenegger, N. Kawai, H. Kjeldsen, G. Laughlin, A. M. Levine, D. Lin, J. J. Lissauer,  
 379    P. MacQueen, G. Marcy, P. R. McCullough, T. D. Morton, N. Narita, M. Paegert, E. Palle, F. Pepe,  
 380    J. Pepper, A. Quirrenbach, S. A. Rinehart, D. Sasselov, B. Sato, S. Seager, A. Sozzetti, K. G. Stassun,  
 381    P. Sullivan, A. Szentgyorgyi, G. Torres, S. Udry, and J. Villasenor, "Transiting Exoplanet Survey  
 382    Satellite (TESS)," Journal of Astronomical Telescopes, Instruments, and Systems 1, p. 014003, Jan.  
 383    2015.
- 384    8 J. Bradbury, R. Frostig, P. Hawkins, M. J. Johnson, C. Leary, D. Maclaurin, and S. Wanderman-Milne,  
 385    "JAX: composable transformations of Python+NumPy programs," 2018.

- 386 9 C. C. Margossian, "A Review of automatic differentiation and its efficient implementation," arXiv e-  
 387 prints , p. arXiv:1811.05031, Nov. 2018.
- 388 10 M. Betancourt, "A Conceptual Introduction to Hamiltonian Monte Carlo," arXiv e-prints ,  
 389 p. arXiv:1701.02434, Jan. 2017.
- 390 11 R. Luger, M. Bedell, D. Foreman-Mackey, I. J. M. Crossfield, L. L. Zhao, and D. W. Hogg, "Mapping  
 391 stellar surfaces III: An Efficient, Scalable, and Open-Source Doppler Imaging Model," arXiv e-prints ,  
 392 p. arXiv:2110.06271, Oct. 2021.
- 393 12 B. P. Bowler, "Imaging Extrasolar Giant Planets," PASP 128, p. 102001, Oct. 2016.
- 394 13 Y. Shechtman, A. Beck, and Y. C. Eldar, "GESPAR: Efficient phase retrieval of sparse signals," IEEE  
 395 Transactions on Signal Processing 62(4), pp. 928–938, 2014.
- 396 14 A. H. Barnett, C. L. Epstein, L. F. Greengard, and J. F. Magland, "Geometry of the phase retrieval  
 397 problem," Inverse Problems 36, p. 094003, sep 2020.
- 398 15 R. W. Gerchberg and W. O. Saxton, "A Practical Algorithm for the Determination of Phase from Image  
 399 and Diffraction Plane Pictures," Optik 35(2), pp. 237–246, 1972.
- 400 16 E. J. Candes, Y. Eldar, T. Strohmer, and V. Voroninski, "Phase Retrieval via Matrix Completion,"  
 401 arXiv e-prints , p. arXiv:1109.0573, Sept. 2011.
- 402 17 C. Metzler, P. Schniter, A. Veeraraghavan, and richard baraniuk, "prDeep: Robust phase retrieval with  
 403 a flexible deep network," in Proceedings of the 35th International Conference on Machine Learning,  
 404 J. Dy and A. Krause, eds., Proceedings of Machine Learning Research 80, pp. 3501–3510, PMLR,  
 405 (Stockholmsmässan, Stockholm Sweden), 10–15 Jul 2018.
- 406 18 Çağatay Işıl, F. S. Oktem, and A. Koç, "Deep iterative reconstruction for phase retrieval," Appl. Opt. 58,  
 407 pp. 5422–5431, Jul 2019.
- 408 19 Y. Nishizaki, R. Horisaki, K. Kitaguchi, M. Saito, and J. Tanida, "Analysis of non-iterative phase  
 409 retrieval based on machine learning," Optical Review 27(1), pp. 136–141, 2020.
- 410 20 J. R. Fienup, J. C. Marron, T. J. Schulz, and J. H. Seldin, "Hubble Space Telescope characterized by  
 411 using phase-retrieval algorithms," Applied Optics 32, pp. 1747–1767, Apr. 1993.
- 412 21 A. S. Jurling and J. R. Fienup, "Applications of algorithmic differentiation to phase retrieval algorithms,"  
 413 J. Opt. Soc. Am. A 31, pp. 1348–1359, Jul 2014.
- 414 22 A. Wong, B. Pope, L. Desdoigts, P. Tuthill, B. Norris, and C. Betters, "Phase retrieval and design with  
 415 automatic differentiation: tutorial," Journal of the Optical Society of America B 38, p. 2465, Aug 2021.
- 416 23 L. Desdoigts, B. Pope, and P. Tuthill, "Optical design, analysis, and calibration using  $\partial$ lux," in Space  
 417 Telescopes and Instrumentation 2022: Optical, Infrared, and Millimeter Wave, L. E. Coyle, M. D.  
 418 Perrin, and S. Matsuura, eds., SPIE, Aug. 2022.
- 419 24 S. B. Howell, C. Sobeck, M. Haas, M. Still, T. Barclay, F. Mullally, J. Troeltzsch, S. Aigrain, S. T.  
 420 Bryson, D. Caldwell, W. J. Chaplin, W. D. Cochran, D. Huber, G. W. Marcy, A. Miglio, J. R. Najita,  
 421 M. Smith, J. D. Twicken, and J. J. Fortney, "The K2 mission: Characterization and early results,"  
 422 Publications of the Astronomical Society of the Pacific 126, p. 398–408, Apr 2014.
- 423 25 G. R. Ricker, J. N. Winn, R. Vanderspek, D. W. Latham, G. Á. Bakos, J. L. Bean, Z. K. Berta-  
 424 Thompson, T. M. Brown, L. Buchhave, N. R. Butler, R. P. Butler, W. J. Chaplin, D. Charbonneau,  
 425 J. Christensen-Dalsgaard, M. Clampin, D. Deming, J. Doty, N. De Lee, C. Dressing, E. W. Dunham,  
 426 M. Endl, F. Fressin, J. Ge, T. Henning, M. J. Holman, A. W. Howard, S. Ida, J. M. Jenkins, G. Jernigan,  
 427 J. A. Johnson, L. Kaltenegger, N. Kawai, H. Kjeldsen, G. Laughlin, A. M. Levine, D. Lin, J. J. Lissauer,  
 428 P. MacQueen, G. Marcy, P. R. McCullough, T. D. Morton, N. Narita, M. Paegert, E. Palle, F. Pepe,  
 429 J. Pepper, A. Quirrenbach, S. A. Rinehart, D. Sasselov, B. Sato, S. Seager, A. Sozzetti, K. G. Stassun,  
 430 P. Sullivan, A. Szentgyorgyi, G. Torres, S. Udry, and J. Villasenor, "Transiting Exoplanet Survey  
 431 Satellite (TESS)," Journal of Astronomical Telescopes, Instruments, and Systems 1, p. 014003, Jan.  
 432 2015.
- 433 26 C. Broeg, A. Fortier, D. Ehrenreich, Y. Alibert, W. Baumjohann, W. Benz, M. Deleuil, M. Gillon,  
 434 A. Ivanov, R. Liseau, M. Meyer, G. Olofsson, I. Pagano, G. Piotto, D. Pollacco, D. Queloz, R. Ragazzoni,  
 435 E. Renotte, M. Steller, and N. Thomas, "CHEOPS: A transit photometry mission for esa's small mission  
 436 programme," EPJ Web of Conferences 47, p. 03005, 2013.
- 437 27 W. Zhu and S. Dong, "Exoplanet statistics and theoretical implications," Annual Review of Astronomy  
 438 and Astrophysics 59, pp. 291–336, Sept. 2021.

- 439 28 C. Aerts, “Probing the interior physics of stars through asteroseismology,” Rev. Mod. Phys. 93,  
 440 p. 015001, Jan 2021.
- 441 29 J. Jackiewicz, “Solar-like oscillators in the kepler era: A review,” Frontiers in Astronomy and Space  
 442 Sciences 7, Mar. 2021.
- 443 30 A. Vanderburg and J. A. Johnson, “A technique for extracting highly precise photometry for the two-  
 444 wheeledkeplermission,” Publications of the Astronomical Society of the Pacific 126, p. 948–958, Oct  
 445 2014.
- 446 31 S. Aigrain, H. Parviainen, and B. J. S. Pope, “K2SC: flexible systematics correction and detrending of  
 447 K2 light curves using Gaussian process regression,” MNRAS 459, pp. 2408–2419, July 2016.
- 448 32 C. E. Rasmussen and C. K. I. Williams, Gaussian Processes for Machine Learning, The MIT Press,  
 449 2005.
- 450 33 S. Aigrain and D. Foreman-Mackey, “Gaussian Process regression for astronomical time-series,” arXiv  
 451 e-prints , p. arXiv:2209.08940, Sept. 2022.
- 452 34 D. Wang, D. W. Hogg, D. Foreman-Mackey, and B. Schölkopf, “A causal, data-driven approach to  
 453 modeling the Kepler data,” Publications of the Astronomical Society of the Pacific 128, p. 094503, Jun  
 454 2016.
- 455 35 R. Luger, E. Agol, E. Kruse, R. Barnes, A. Becker, D. Foreman-Mackey, and D. Deming, “EVEREST:  
 456 Pixel level decorrelation of K2 light curves,” The Astronomical Journal 152, p. 100, Oct 2016.
- 457 36 T. R. White, B. J. S. Pope, V. Antoci, P. I. Pápics, C. Aerts, D. R. Gies, K. Gordon, D. Huber,  
 458 G. H. Schaefer, S. Aigrain, S. Albrecht, T. Barclay, G. Barentsen, P. G. Beck, T. R. Bedding, M. Fred-  
 459 slund Andersen, F. Grundahl, S. B. Howell, M. J. Ireland, S. J. Murphy, M. B. Nielsen, V. Silva Aguirre,  
 460 and P. G. Tuthill, “Beyond the Kepler/K2 bright limit: variability in the seven brightest members of  
 461 the Pleiades,” Monthly Notices of the Royal Astronomical Society 471, p. 2882–2901, Aug 2017.
- 462 37 B. J. S. Pope, T. R. White, W. M. Farr, J. Yu, M. Greklek-McKeon, D. Huber, C. Aerts, S. Aigrain,  
 463 T. R. Bedding, T. Boyajian, O. L. Creevey, and D. W. Hogg, “The K2 bright star survey. I. Methodology  
 464 and Data Release,” The Astrophysical Journal Supplement Series 245, p. 8, Nov 2019.
- 465 38 J. Kammerer, M. J. Ireland, F. Martinache, and J. H. Girard, “Kernel phase imaging with VLT/-  
 466 NACO: high-contrast detection of new candidate low-mass stellar companions at the diffraction limit,”  
 467 MNRAS 486, pp. 639–654, June 2019.
- 468 39 Euclid Collaboration, A. S. Borlaff, P. Gómez-Alvarez, B. Altieri, P. M. Marcum, R. Vavrek, R. Laureijs,  
 469 R. Kohley, F. Buitrago, J. C. Cuillandre, P. A. Duc, L. M. Gaspar Venancio, A. Amara, S. Andreon,  
 470 N. Auricchio, R. Azzollini, C. Baccigalupi, A. Balaguera-Antolínez, M. Baldi, S. Bardelli, R. Bender,  
 471 A. Biviano, C. Bodendorf, D. Bonino, E. Bozzo, E. Branchini, M. Brescia, J. Brinchmann, C. Burigana,  
 472 R. Cabanac, S. Camera, G. P. Candini, V. Capobianco, A. Cappi, C. Carbone, J. Carretero, C. S.  
 473 Carvalho, S. Casas, F. J. Castander, M. Castellano, G. Castignani, S. Cavuoti, A. Cimatti, R. Cledas-  
 474 sou, C. Colodro-Conde, G. Congedo, C. J. Conselice, L. Conversi, Y. Copin, L. Corcione, J. Coupon,  
 475 H. M. Courtois, M. Cropper, A. Da Silva, H. Degaudenzi, D. Di Ferdinando, M. Doussis, F. Dubath,  
 476 C. A. J. Duncan, X. Dupac, S. Dusini, A. Ealet, M. Fabricius, M. Farina, S. Farrens, P. G. Ferreira,  
 477 S. Ferriol, F. Finelli, P. Flose-Reimberg, P. Fosalba, M. Frailis, E. Franceschi, M. Fumana, S. Gale-  
 478 otta, K. Ganga, B. Garilli, B. Gillis, C. Giocoli, G. Gozaliasl, J. Graciá-Carpio, A. Grazian, F. Grupp,  
 479 S. V. H. Haugan, W. Holmes, F. Hormuth, K. Jahnke, E. Keihanen, S. Kermiche, A. Kiessling, M. Kil-  
 480 binger, C. C. Kirkpatrick, T. Kitching, J. H. Knapen, B. Kubik, M. Kümmel, M. Kunz, H. Kurki-  
 481 Suonio, P. Liebing, S. Ligori, P. B. Lilje, V. Lindholm, I. Lloro, G. Mainetti, D. Maino, O. Mansutti,  
 482 O. Marggraf, K. Markovic, M. Martinelli, N. Martinet, D. Martínez-Delgado, F. Marulli, R. Massey,  
 483 M. Maturi, S. Maurogordato, E. Medinaceli, S. Mei, M. Meneghetti, E. Merlin, R. B. Metcalf, G. Mey-  
 484 lan, M. Moresco, G. Morgante, L. Moscardini, E. Munari, R. Nakajima, C. Neissner, S. M. Niemi, J. W.  
 485 Nightingale, A. Nucita, C. Padilla, S. Paltani, F. Pasian, L. Patrizii, K. Pedersen, W. J. Percival, V. Pet-  
 486 torino, S. Pires, M. Poncet, L. Popa, D. Potter, L. Pozzetti, F. Raison, R. Rebolo, A. Renzi, J. Rhodes,  
 487 G. Riccio, E. Romelli, M. Roncarelli, C. Rosset, E. Rossetti, R. Saglia, A. G. Sánchez, D. Sapone,  
 488 M. Sauvage, P. Schneider, V. Scottez, A. Secroun, G. Seidel, S. Serrano, C. Sirignano, G. Sirri, J. Skot-  
 489 tfelt, L. Stanco, J. L. Starck, F. Sureau, P. Tallada-Crespi, A. N. Taylor, M. Tenti, I. Tereno, R. Teyssier,  
 490 R. Toledo-Moreo, F. Torradeflot, I. Tutusaus, E. A. Valentijn, L. Valenziano, J. Valiviita, T. Vassallo,

- 491 M. Viel, Y. Wang, J. Weller, L. Whittaker, A. Zacchei, G. Zamorani, and E. Zucca, “Euclid preparation.  
 492 XVI. Exploring the ultra-low surface brightness Universe with Euclid/VIS,” *A&A* 657, p. A92,  
 493 Jan. 2022.
- 494 40 M. D. Perrin, R. Soummer, E. M. Elliott, M. D. Lallo, and A. Sivaramakrishnan, Simulating point spread  
 495 functions for the James Webb Space Telescope with WebbPSF, vol. 8442 of Society of Photo-Optical  
 496 Instrumentation Engineers (SPIE) Conference Series, p. 84423D. 2012.
- 497 41 M. D. Perrin, A. Sivaramakrishnan, C.-P. Lajoie, E. Elliott, L. Pueyo, S. Ravindranath, and L. Albert,  
 498 “Updated point spread function simulations for JWST with WebbPSF,” in *Space Telescopes and In-*  
 499 *strumentation 2014: Optical, Infrared, and Millimeter Wave*, J. Oschmann, Jacobus M., M. Clampin,  
 500 G. G. Fazio, and H. A. MacEwen, eds., Society of Photo-Optical Instrumentation Engineers (SPIE)  
 501 Conference Series 9143, p. 91433X, Aug. 2014.
- 502 42 N. Metropolis, A. W. Rosenbluth, M. N. Rosenbluth, A. H. Teller, and E. Teller, “Equation of state  
 503 calculations by fast computing machines,” *The Journal of Chemical Physics* 21, pp. 1087–1092, June  
 504 1953.
- 505 43 D. Huijser, J. Goodman, and B. J. Brewer, “Properties of the affine-invariant ensemble sampler’s ‘stretch  
 506 move’ in high dimensions,” *Australian & New Zealand Journal of Statistics* 64, pp. 1–26, Feb. 2022.
- 507 44 Y. LeCun, Y. Bengio, and G. Hinton, “Deep learning,” *Nature* 521, pp. 436–444, May 2015.
- 508 45 Theano Development Team, “Theano: A Python framework for fast computation of mathematical  
 509 expressions,” arXiv e-prints abs/1605.02688, May 2016.
- 510 46 M. Abadi, A. Agarwal, P. Barham, E. Brevdo, Z. Chen, C. Citro, G. S. Corrado, A. Davis, J. Dean,  
 511 M. Devin, S. Ghemawat, I. Goodfellow, A. Harp, G. Irving, M. Isard, Y. Jia, R. Jozefowicz, L. Kaiser,  
 512 M. Kudlur, J. Levenberg, D. Mané, R. Monga, S. Moore, D. Murray, C. Olah, M. Schuster, J. Shlens,  
 513 B. Steiner, I. Sutskever, K. Talwar, P. Tucker, V. Vanhoucke, V. Vasudevan, F. Viégas, O. Vinyals,  
 514 P. Warden, M. Wattenberg, M. Wicke, Y. Yu, and X. Zheng, “TensorFlow: Large-scale machine learning  
 515 on heterogeneous systems,” 2015. Software available from tensorflow.org.
- 516 47 A. Paszke, S. Gross, F. Massa, A. Lerer, J. Bradbury, G. Chanan, T. Killeen, Z. Lin, N. Gimelshein,  
 517 L. Antiga, A. Desmaison, A. Köpf, E. Yang, Z. DeVito, M. Raison, A. Tejani, S. Chilamkurthy,  
 518 B. Steiner, L. Fang, J. Bai, and S. Chintala, “PyTorch: An Imperative Style, High-Performance Deep  
 519 Learning Library,” arXiv e-prints , p. arXiv:1912.01703, Dec. 2019.
- 520 48 J. Bezanson, S. Karpinski, V. B. Shah, and A. Edelman, “Julia: A Fast Dynamic Language for Technical  
 521 Computing,” arXiv e-prints , p. arXiv:1209.5145, Sep 2012.
- 522 49 C. R. Harris, K. J. Millman, S. J. van der Walt, R. Gommers, P. Virtanen, D. Cournapeau, E. Wieser,  
 523 J. Taylor, S. Berg, N. J. Smith, R. Kern, M. Picus, S. Hoyer, M. H. van Kerkwijk, M. Brett, A. Haldane,  
 524 J. F. del Río, M. Wiebe, P. Peterson, P. Gérard-Marchant, K. Sheppard, T. Reddy, W. Weckesser,  
 525 H. Abbasi, C. Gohlke, and T. E. Oliphant, “Array programming with NumPy,” *Nature* 585(7825),  
 526 pp. 357–362, 2020.
- 527 50 B. J. S. Pope, L. Pueyo, Y. Xin, and P. G. Tuthill, “Kernel phase and coronagraphy with automatic  
 528 differentiation,” *The Astrophysical Journal* 907, p. 40, jan 2021.
- 529 51 P. Kidger and C. Garcia, “Equinox: neural networks in JAX via callable PyTrees and filtered trans-  
 530 formations,” Differentiable Programming workshop at Neural Information Processing Systems 2021 ,  
 531 2021.
- 532 52 M. Hessel, D. Budden, F. Viola, M. Rosca, E. Sezener, and T. Hennigan, “Optax: composable gradient  
 533 transformation and optimisation, in jax!,” 2020.
- 534 53 D. Phan, N. Pradhan, and M. Jankowiak, “Composable Effects for Flexible and Accelerated Probabilistic  
 535 Programming in NumPyro,” arXiv e-prints , p. arXiv:1912.11554, Dec. 2019.
- 536 54 J. Page and P. Favaro, “Learning to Model and Calibrate Optics via a Differentiable Wave Optics  
 537 Simulator,” arXiv e-prints , p. arXiv:2005.08562, May 2020.
- 538 55 V. Sitzmann, S. Diamond, Y. Peng, X. Dun, S. Boyd, W. Heidrich, F. Heide, and G. Wetzstein,  
 539 “End-to-end optimization of optics and image processing for achromatic extended depth of field and  
 540 super-resolution imaging,” *ACM Trans. Graph.* 37, July 2018.
- 541 56 T. Liaudat, J.-L. Starck, M. Kilbinger, and P.-A. Frugier, “Rethinking the modeling of the instrumental  
 542 response of telescopes with a differentiable optical model,” arXiv e-prints , p. arXiv:2111.12541, Nov.  
 543 2021.

- 544 57 T. Liaudat, J.-L. Starck, M. Kilbinger, and P.-A. Frugier, "Rethinking data-driven point spread function  
 545 modeling with a differentiable optical model," arXiv e-prints , p. arXiv:2203.04908, Mar. 2022.
- 546 58 G. Stefansson, S. Mahadevan, L. Hebb, J. Wisniewski, J. Huehnerhoff, B. Morris, S. Halverson, M. Zhao,  
 547 J. Wright, J. O'rourke, H. Knutson, S. Hawley, S. Kanodia, Y. Li, L. M. Z. Hagen, L. J. Liu, T. Beatty,  
 548 C. Bender, P. Robertson, J. Dembicky, C. Gray, W. Ketzeback, R. McMillan, and T. Rudyk, "Toward  
 549 Space-like Photometric Precision from the Ground with Beam-shaping Diffusers," ApJ 848, p. 9, Oct.  
 550 2017.
- 551 59 F. Martinache, "The Asymmetric Pupil Fourier Wavefront Sensor," PASP 125, p. 422, Apr. 2013.
- 552 60 R. Soummer, L. Pueyo, A. Sivaramakrishnan, and R. J. Vanderbei, "Fast computation of Lyot-style  
 553 coronagraph propagation," Optics Express 15, p. 15935, Jan. 2007.
- 554 61 F. Martinache, A. Ceau, R. Laugier, J. Kammerer, M. N'Diaye, D. Mary, N. Cvetojevic, and C. Lopez,  
 555 "Kernel-phase analysis: Aperture modeling prescriptions that minimize calibration errors," A&A 636,  
 556 p. A72, Apr. 2020.
- 557 62 D. P. Kingma and J. Ba, "Adam: A Method for Stochastic Optimization," arXiv e-prints ,  
 558 p. arXiv:1412.6980, Dec. 2014.
- 559 63 Y. Bard, "Nonlinear parameter estimation," tech. rep., 1974.
- 560 64 J. F. P. d. Costa, Weighted Correlation, pp. 1653–1655. Springer Berlin Heidelberg, Berlin, Heidelberg,  
 561 2011.
- 562 65 T. Pinder and D. Dodd, "GPJax: A Gaussian Process framework in JAX," Journal of Open Source  
 563 Software 7(75), p. 4455, 2022.
- 564 66 W. Zhu, C. X. Huang, A. Udalski, M. Soares-Furtado, R. Poleski, J. Skowron, P. Mróz, M. K. Szymański,  
 565 I. Soszyński, P. Pietrukowicz, S. Kozłowski, K. Ulaczyk, and M. Pawlak, "Extracting Microlensing  
 566 Signals from K2 Campaign 9," PASP 129, p. 104501, Oct. 2017.
- 567 67 D. Nardiello, L. Borsato, G. Piotto, L. S. Colombo, E. E. Manthopoulou, L. R. Bedin, V. Granata,  
 568 G. Lacedelli, M. Libralato, L. Malavolta, M. Montalto, and V. Nascimbeni, "A PSF-based Approach to  
 569 TESS High quality data Of Stellar clusters (PATHOS) - I. Search for exoplanets and variable stars in  
 570 the field of 47 Tuc," MNRAS 490, pp. 3806–3823, Dec. 2019.
- 571 68 C. Hedges, R. Luger, J. Martinez-Palomera, J. Dotson, and G. Barentsen, "Linearized Field Deblending:  
 572 Point-spread Function Photometry for Impatient Astronomers," AJ 162, p. 107, Sept. 2021.
- 573 69 M. E. Higgins and K. J. Bell, "Localizing Sources of Variability in Crowded TESS Photometry," arXiv  
 574 e-prints , p. arXiv:2204.06020, Apr. 2022.
- 575 70 O. Guyon, E. A. Bendek, J. A. Eisner, R. Angel, N. J. Woolf, T. D. Milster, S. M. Ammons, M. Shao,  
 576 S. Shaklan, M. Levine, B. Nemati, J. Pitman, R. A. Woodruff, and R. Belikov, "High-precision Astrometry  
 577 with a Diffractive Pupil Telescope," ApJS 200, p. 11, June 2012.
- 578 71 O. Guyon, J. A. Eisner, R. Angel, N. J. Woolf, E. A. Bendek, T. D. Milster, S. M. Ammons, M. Shao,  
 579 S. Shaklan, M. Levine, B. Nemati, F. Martinache, J. Pitman, R. A. Woodruff, and R. Belikov, "Simultaneous  
 580 Exoplanet Characterization and Deep Wide-field Imaging with a Diffractive Pupil Telescope,"  
 581 ApJ 767, p. 11, Apr. 2013.
- 582 72 J. P. Gardner, J. C. Mather, M. Clampin, R. Doyon, M. A. Greenhouse, H. B. Hammel, J. B. Hutchings,  
 583 P. Jakobsen, S. J. Lilly, K. S. Long, J. I. Lunine, M. J. McCaughrean, M. Mountain, J. Nella, G. H. Rieke,  
 584 M. J. Rieke, H.-W. Rix, E. P. Smith, G. Sonneborn, M. Stiavelli, H. S. Stockman, R. A. Windhorst,  
 585 and G. S. Wright, "The James Webb Space Telescope," SSRv 123, pp. 485–606, Apr. 2006.
- 586 73 R. T. Zellem, B. Nemati, G. Gonzalez, M. Ygouf, V. P. Bailey, E. J. Cady, M. M. Colavita, S. R.  
 587 Hildebrandt, E. R. Maier, B. Mennesson, L. Payne, N. T. Zimmerman, R. Belikov, R. J. De Rosa,  
 588 J. Debes, E. S. Douglas, J. Girard, T. Groff, J. Kasdin, P. J. Lowrance, B. Macintosh, D. Ryan, and  
 589 C. Weisberg, "Nancy Grace Roman Space Telescope coronagraph instrument observation calibration  
 590 plan," in Space Telescopes and Instrumentation 2022: Optical, Infrared, and Millimeter Wave, L. E.  
 591 Coyle, S. Matsuura, and M. D. Perrin, eds., Society of Photo-Optical Instrumentation Engineers (SPIE)  
 592 Conference Series 12180, p. 121801Z, Aug. 2022.

- 593 74 F. Cantalloube, C. Gomez-Gonzalez, O. Absil, C. Cantero, R. Bacher, M. J. Bonse, M. Bottom, C. H.  
594 Dahlqvist, C. Desgrange, O. Flasseur, T. Fuhrmann, T. Henning, R. Jensen-Clem, M. Kenworthy,  
595 D. Mawet, D. Mesa, T. Meshkat, D. Mouillet, A. Mueller, E. Nasedkin, B. Pairet, S. Pierard, J. B. Ruffio,  
596 M. Samland, J. Stone, and M. Van Droogenbroeck, “Exoplanet Imaging Data Challenge: benchmarking  
597 the various image processing methods for exoplanet detection,” arXiv e-prints , p. arXiv:2101.05080,  
598 Jan. 2021.
- 599 75 Z. Rustamkulov, D. K. Sing, R. Liu, and A. Wang, “Analysis of a JWST NIRSpec lab time series:  
600 Characterizing systematics, recovering exoplanet transit spectroscopy, and constraining a noise floor,”  
601 The Astrophysical Journal Letters 928, p. L7, Mar. 2022.
- 602 76 D. Coe, “Fisher Matrices and Confidence Ellipses: A Quick-Start Guide and Software,” arXiv e-prints  
603 , p. arXiv:0906.4123, June 2009.
- 604 77 J. D. Hunter, “Matplotlib: A 2d graphics environment,” Computing In Science & Engineering 9(3),  
605 pp. 90–95, 2007.